Spring 5-10-2020

A Method to Reclaim Multifractal Statistics from Saturated Images

Jeremy Juybari
University of Maine, jeremy.juybari@maine.edu

A METHOD TO RECLAIM MULTIFRACTAL STATISTICS FROM SATURATED IMAGES

By

Jeremy Bijan Juybari

B.A., San Diego State University 2017

A THESIS

Submitted in Partial Fulfillment of the

Requirements for the Degree of

Master of Arts

(in Mathematics)

The Graduate School

The University of Maine

May 2020

Advisory Committee:

Dr. Andre Khalil, Associate Professor of Biomedical Engineering, Co-Advisor

Dr. David Bradley, Associate Professor of Mathematics, Co-Advisor

Dr. Peter Stechlinski, Associate Professor of Mathematics

A METHOD TO RECLAIM MULTIFRACTAL STATISTICS FROM SATURATED IMAGES

By Jeremy Bijan Juybari

Thesis Co-Advisors: Dr. Andre Khalil and Dr. David Bradley

An Abstract of the Thesis Presented
in Partial Fulfillment of the Requirements for the
Degree of Master of Arts
(in Mathematics)
May 2020

The CompuMAINE lab has developed a patented computational cancer detection method utilizing the 2D Wavelet Transform Modulus Maxima (WTMM) method to help predict disrupted, tumor-associated breast tissue from mammography. The lab has a database of mammograms in which some of the image subregions contain artifacts which are excluded from the analysis, image saturation is one such artefact. These rejected image subregions reduce the number of statistics for a given image hence decreasing the statistical power of clinical analyses. Thus our goal is therefore to minimize the rejection of image subregions containing artifacts. The aim of this particular project is to explore the effects of image saturation on the resulting multifractal statistics from the 2D WTMM method. Groups of numerically simulated (monofractal) fractional Brownian motion (fBm) surfaces with varying roughness exponents were generated and saturated at the 1%, 5%, 10% and 20% levels. We find that image saturation reduces the range of available statistical order moments relative to an unsaturated image. By assessing the effects of image saturation on the 2D WTMM calculations, we developed a filtering approach where we nearly regained the entire range of statistical order moments thus limiting the impacts of image saturation.

TABLE OF CONTENTS

LIST OF FIGURES

CHAPTER 1

INTRODUCTION

The radiological interpretation of mammograms in diagnosing breast cancer is a complex task, since normal mammographic tissue varies in its structure. Mammograms are either processed by two expert radiologists or a radiologist in conjunction with a Computer Aided Detection (CAD) method. The Federal Food And Drug Administration, approved CAD methods for breast cancer in the 1990s; the period from 2002 to 2016 saw the widespread adoption of CAD from 3% to 92% [12, 19]. However promising CAD methods failed performance expectations [11]: they are associated with decreased specificity (decreased accuracy in diagnostic tests) [10], increased recall rates of healthy women (a diagnostic check-in from a previous mammogram) [8, 12, 25] and a false-positive rate on up to 70% [18]. The chief medical officer of the American Cancer Society in 2017 stated "we have a phenomenon of over diagnosis" [26].

A powerful risk factor in diagnosing breast cancer, is breast density with dense breast tissue used as a competent predictor [28]. A common metric for breast density is the percent mammographic density (PMD) which, when added to breast cancer risk models, improved the prediction rate [20]. The CompuMAINE research lab, colloquially known as the lab, has developed an alternative risk factor, based upon biophysical processes that previous research has not considered, utilizing breast tissue disruption. The patented computational cancer detection method implements the 2D Wavelet Transform Modulus Maxima (WTMM) method [16].

The 2D WTMM method is a multiscale multifractal formalism perfectly suited for the analysis of self-affine rough surfaces such as mammograms by identifying density fluctuations and spatial correlations within these surfaces. [2, 4, 7, 15, 17, 24, 27]. The Hölder exponent locally quantifies these correlations as a multifractal while the Hurst exponent

globally quantifies these correlations as a monofractal. Image subregions from mammograms (breast tissue regions) compelling display monofractal fluctuations permitting the use of the the Hurst exponent (H). The lab has classified three types of mammographic breast tissue based upon the correlation they exhibit: fatty tissue ($H \leq 0.45$), dense tissue ($H \geq 0.55$) and disrupted tissue ($0.45 < H < 0.55$) [24]. This process is displayed in Figure 1.1 with yellow for disrupted tissue, red for dense tissue and blue for fatty tissue.

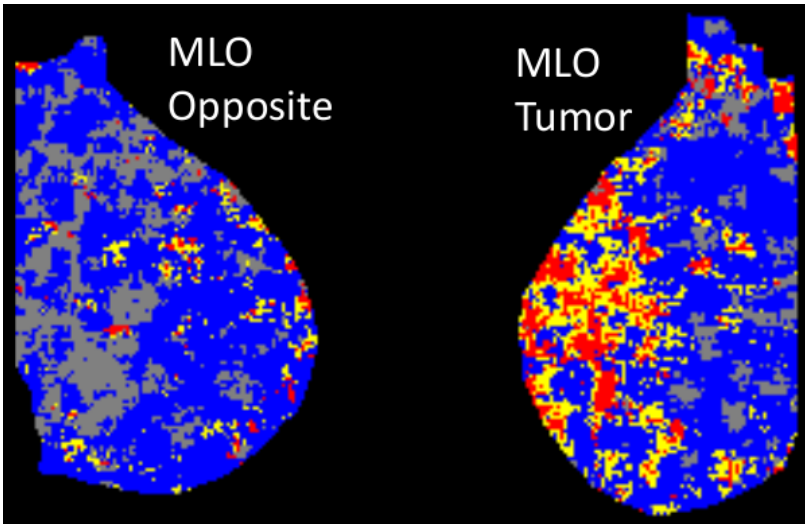

Figure 1.1: Example of the output from the CompuMAINE lab patented algorithm on a mammogram. Each color corresponds to a different type of fractal signature for that image subregion: $0.45 < H < 0.55$ for disrupted tissue (yellow), $H \geq 0.55$ for dense tissue (red), $H \leq 0.45$ for fatty tissue (blue). Observe that the tumorous breast has more yellow squares than the opposite, non-tumorous, breast. MLO stands for the mediolateral oblique view which is a specific angle at which the mammogram is captured. The gray regions correspond to image subregions that were excluded.

The importance of these results is that they are not solely numerical, there is a biophysical basis. The yellow squares in Figure 1.1 corresponding to disrupted breast tissue, were principally located in tumorous breasts. A signature of $H \sim 0.5$ is associated with coin-flip randomness and a lack of spatial correlation. Furthermore previous researchers found that malignant cells are associated with loss of cellular coherent angular motion [5, 31]. Thus it is hypothesized that tissue disruption (yellow squares) is also associated with $H \sim 0.5$.

However, some of the mammograms in the lab's database contain image subregion artifacts. The gray regions in Figure 1.1 are such subregions, where we could not determine the fractal signature. Since regions are then excluded from the analysis, our goal is to minimize the rejection of image subregions containing such artifacts in order to maximize statistical power in our clinical analyses.

One such artifact is saturation, an over abundance of pixels that have greatest pixel value. By empirically exploring the effect of image saturation we were able to develop a method that is analogous to a vaccine: effects from image saturation were eliminated from the analysis while at the same, the method only had negligible effects on control (non-saturated) images. We refer to this as the rescue method. This technique did not previously exist in the literature or the CompuMAINE lab's patented algorithm. The rescue method is a novel approach to mitigate the effects of image saturation and it will be used in combination with the lab's algorithm. Future work would focus on other image artifacts.

1.1 Image Saturation

Image saturation is when an image has a greater proportion of pixels at a specific value relative to the unsaturated (normal) image. For example, an unsigned 32 bit gray scale image will have pixel values ranging from 0 to $2^{32} - 1$. A pixel value of 0 corresponds to black and the max value corresponds to white, while other values are various shades of gray. Image saturation means that there is a greater density of pixels at the max value relative to an unsaturated image. For this research we saturated images by looking at the cumulative density function of the pixel values for a specific image, then determined the corresponding pixel for a desired percentile and saturated all pixels in the percentile or higher.

For instance, to ensure that an image has 20% saturation, we find the pixel value at the 80^{th} percentile and then make all those pixels that have this pixel value or higher the max

pixel value (pure white). This image is then considered 20% saturated. Observe that any information about shading among those values is lost. An analogy is to compare image saturation to cutting off the tops of mountains. The portion of mountain removed also removes the corresponding information about elevation.

Figure 1.2 shows fractional Brownian motion surfaces (fBms) for $H = 0.1, 0.3, 0.5, 0.7$ and saturation for each image at the 20% level. The statistical tendencies of the Hurst exponent are visible moving from Figure 1.2 (a) to (d). In this context, $H = 0.1$ means that low pixel values tend to be followed by larger values (antipersistant) while $H = 0.7$ means that large pixel values tend to stay large (long-range correlated) and similarly, small pixel values tend to stay small. Image roughness is clearly displayed in Figure 1.2 (a) $(H = 0.1)$ compared to Figure 1.2 (d) $(H = 0.7)$ which is a more smooth image. Furthermore, we see that image saturation affects the fractional Brownian motion surfaces differently depending on the Hurst exponent. Larger exponents have the saturated pixels closely clustered together while lower exponents have a more uniform dispersion as shown in Figure 1.3.

Figure 1.4 shows image saturation on a mammogram in the lower left side of the image. The white spot within the black box are pixels that all share the max pixel value of the image, hence they are white. This is an example of an image artifact from saturation that decreases the statistical power of the algorithm.

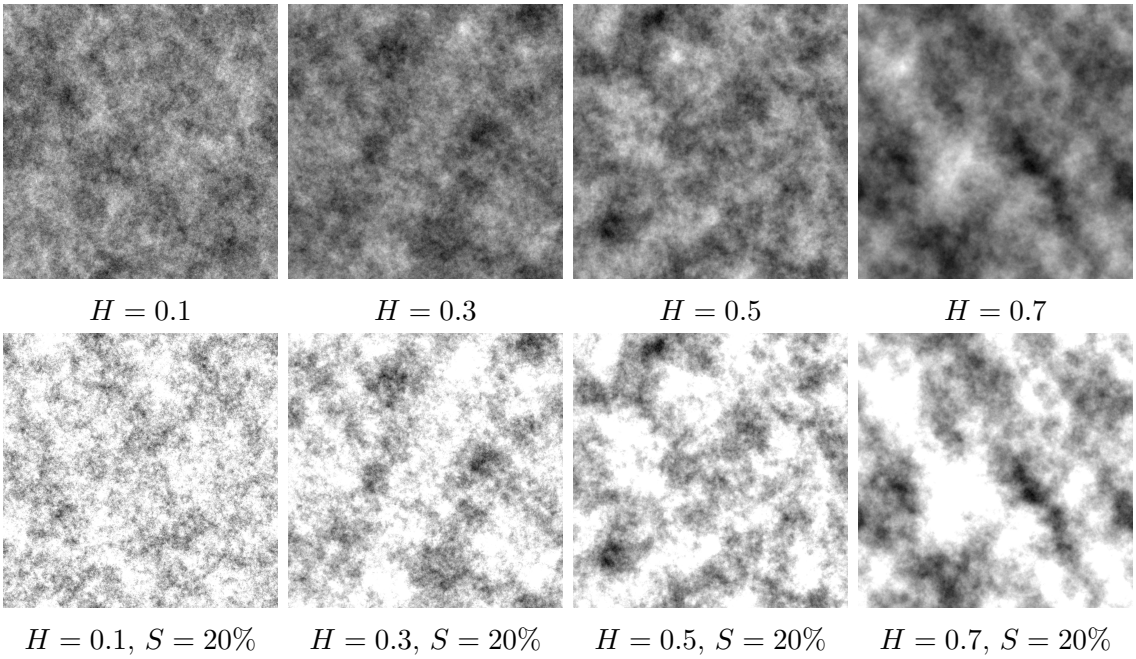

Figure 1.2: The top row shows unsaturated 2D fractional Brownian motion surfaces. Moving left to right, it is possible to see the image becoming more smooth as a function of the Hurst exponent. The second row is the same images but saturated at the 20% level which is the highest level of saturation we numerically simulated.

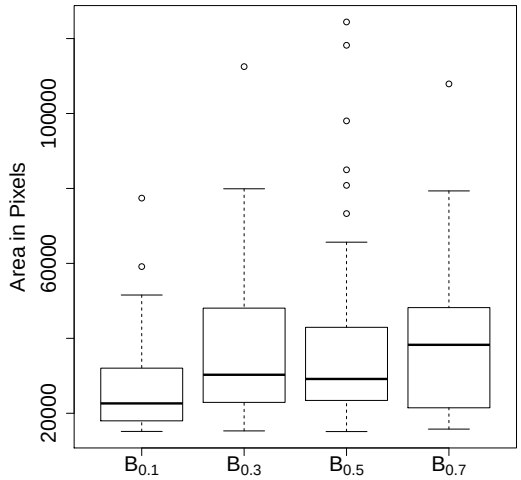

Figure 1.3: A boxplot of the max pixel areas conditioned on the area greater than 15000 pixels, for all the fBms saturated at 20%. The median (black bar) is higher for $B_{0.7}$ than it is for for $B_{0.1}$ which means that fbm surfaces with $H = 0.7$ had more large regions of homogeneous max pixel values.

Figure 1.4: The black box in the lower left portion of the image is showing a region with image saturation (white spots). Such a region leads to a gray subregion in Figure 1.1.

CHAPTER 2

METHODOLOGY

In this chapter we develop the concepts needed for the 2D Wavelet Transform Modulus Maxima (WTMM) method used in this project. We begin with defining a notion of roughness locally then globally, then discussing fractional Brownian motion, the fractal dimension, and multifractals. Lastly we cover the 2D WTMM method.

2.1 Hölder Exponent

The Hölder exponent, also known as a Lipschitz exponent, is a measurement of the strength of a singularity in a signal which could also be called a function. The Hölder exponent is a function of time or space or other independent variables, as a signal can have singularities at points in the signal's domain with different Hölder exponents. We state Taylor's Reminder Theorem and then develop the main definition of this section, from [1], is below

Definition 2.1.1 (Hölder exponent)**.** Let $f : \mathbb{R} \to \mathbb{R}$ be a continuous mapping. f has a Hölder exponent of order $h(x_0)$, the largest possible exponent, at x_0, such that there exists some $C \in \mathbb{R}$, $C > 0$, so that for any point x in some neighborhood of x_0 one has,

$$|f(x) - P_n(x)| \leq C|x - x_0|^{h(x_0)}. \tag{2.1}$$

Remark. Definition 2.1.1 included continuity as a property of the function, which means that $h(x_0) > 0$ otherwise $h(x_0) \leq 0$ is possible with discontinuities present. Note that we are only interested in continuous functions.

Lemma 2.1.1. The possible values for the Hölder exponent in Definition 2.1.1 are $h(x_0) \in (0, 1)$ if f is continuous but not differentiable.

Proof. We proceed by contradiction, let $h(x_0) > 1$, by equation (2.1) we have

$$|f(x) - f(x_0)| \leq C|x - x_0|^{h(x_0)}$$

without loss of generality let $x \neq x_0$,

$$\frac{|f(x) - f(x_0)|}{|x - x_0|} \leq C|x - x_0|^{h(x_0)-1}$$

taking the limit on both sides,

$$\lim_{x \to x_0} \frac{|f(x) - f(x_0)|}{|x - x_0|} \leq \lim_{x \to x_0} C|x - x_0|^{h(x_0)-1}$$

and by the squeeze theorem,

$$|f^{'}(x_0)| \leq 0$$

which is a contradiction as needed since f is not differentiable at x_0. □

However note that if $h(x_0) = 1$ the function is lipschitz continuous and for $h > 1$ the function is differentiable. The estimation of the Hölder exponent is done by using Taylor Polynomials to relate the differentiability of the signal to the polynomial approximation [21, 30].

Definition 2.1.2 (Taylor Polynomials)**.** Let f be an m times differentiable function in $[x_0 - b, x_0 + b]$ for $b > 0$. The mth-order Taylor polynomial for f centered at x_0, denoted $p_{x_0,m}(x)$, has the property that it matches f in value, slope and all derivatives up to the mth derivative,

$$p_{x_0,m}(x_0) = f(x_0), p^{(1)}_{x_0,m}(x_0) = f^{(1)}(x_0), ..., p^{(m)}_{x_0,m}(x_0) = f^{(m)}(x_0).$$

And we have

$$p_{x_0,m}(x) = \sum_{k=0}^{m} \frac{f^{(k)}(x_0)}{k!}(x - x_0)^k. \tag{2.2}$$

We will use Taylor's Remainder Theorem to get an upper bound for the estimate of the remainder.

Theorem 2.1.2 (Taylor's Remainder Theorem)**.** Let f be $m+1$ times differentiable on the interval (a,b), where $x_0 \in (a,b)$. For all $x \in (a,b)$,

$$f(x) = p_{x_0,m}(x) + R_{x_0,m}(x),$$

where $p_{x_0,m}(x)$ is the m th order Taylor polynomial for f centered at x_0 and the remainder is

$$R_{x_0,m}(x) = \frac{f^{(m+1)}(c)}{(m+1)!}(x-x_0)^{m+1}$$

for some point c between x and x_0.

Note that the notation is preserved from [30] by using $m+1$ differentiability, others [21] defined the Taylor Polynomial of order m with $m-1$ instead of m in Eq. (2.2).

Theorem 2.1.3 (Estimate of the Remainder)**.** Let $m \in \mathbb{N}$. The remainder in the mth-order Taylor polynomial for f centered at x_0, for some $d \in \mathbb{R}, d > 0$ satisfies

$$\Big|R_{x_0,m}(x)\Big| = \Big|f(x) - p_{x_0,m}(x)\Big| \leq \frac{|x-x_0|^{m+1}}{(m+1)!} \sup_{u\in[x_0-d,x_0+d]} |f^{m+1}(u)|$$

The following definition of the Hölder exponent comes from Arneodo [1] which is a seminal paper for multifractal analysis with the 2D WTMM method which is the same as 2.1.1.

Definition 2.1.3. *Singular* means a discontinuity in the derivative of the signal.

Definition 2.1.4 (Hölder exponent)**.** A definition of the Hölder exponent, as the strength of the singularity of a function f at the point x_0, is given by the largest exponent $h(x_0)$ such that there exists a Taylor Polynomial $P_n(x)$ of degree $n < h(x_0)$ and a constant $C > 0$, so that for any point x in some neighborhood of x_0,

$$\Big|f(x) - P_n(x)\Big| \leq C\Big|x - x_0\Big|^{h(x_0)}. \tag{2.3}$$

It is possible to design a function that has a Hölder exponent, h, at each point. This means that a function can have the same h at every point or a different h or a collection of Hölder

exponents pertaining to groups of points. This distinction will become very important when discussing monofractal and multifractal signals. Furthermore, from Lemma 2.1.1 we know, if $0 \leq h(x_0) < 1$ then the expression in Eq. (2.3) becomes

$$|f(x) - f(x_0)| \leq C|x - x_0|^{h(x_0)} \tag{2.4}$$

meaning that f is not differentiable at x_0 and $P_n(x) = f(x_0)$.

The following propositions all use Definition 2.1.1 unless otherwise noted.

Proposition 2.1.4. All polynomials have a Hölder exponent of ∞ for any point $x_0 \in \mathbb{R}$.

Proof. Note that for any polynomial the Taylor Polynomial is the polynomial itself. Let $f(x) = P(x)$ be a polynomial and $x_0 \in \mathbb{R}$. By (2.3) we have

$$|f(x) - P_n(x)| \leq C|x - x_0|^{h(x_0)}$$

and by the above note,

$$0 \leq C|x - x_0|^{h(x_0)}$$

which clearly holds for x on any neighborhood of x_0 with $h(x_0)$ any positive number. □

Proposition 2.1.5. Any real analytic function, f, on $\mathbb{R}$ has $h(x_0) = \infty$ for any point $x_0 \in \mathbb{R}$.

Proof. By Eq. (2.3) we have,

$$|f(x) - P_n(x)| \leq C|x - x_0|^{h(x_0)}$$

where n is the order of the Taylor Polynomial from Theorem 2.1.3,

$$\begin{aligned} |f(x) - P_n(x)| &\leq \frac{|x - x_0|^{n+1}}{(n+1)!} \sup_{u \in [x_0 - d, x_0 + d]} |f^{n+1}(u)| \\ &\leq |x - x_0|^{n+1} \sup_{u \in [x_0 - d, x_0 + d]} |f^{n+1}(u)|. \end{aligned}$$

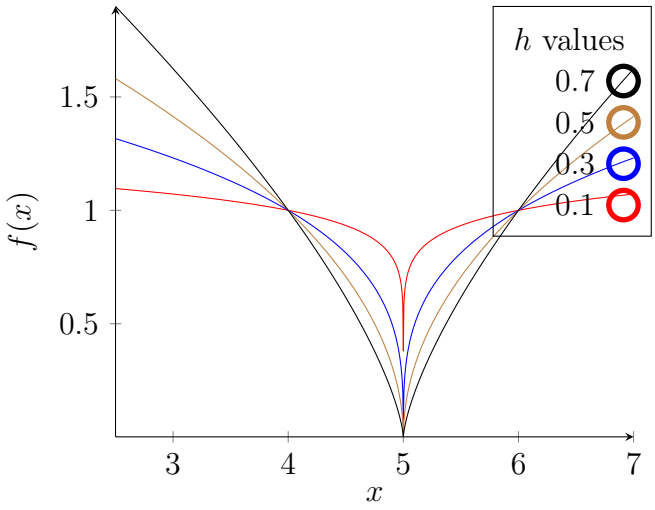

Figure 2.1: A figure showing the different behavior of $h \in (0,1)$ for $f(x) = |x-5|^h$ with $h = 0.1, 0.3, 0.5, 0.7$. As h the strength of the singularity decreases.

Let $C = |x - x_0| \sup_{u \in [x_0-d, x_0+d]} |f^{n+1}(u)|$ and thus

$$|f(x) - P_n(x)| \leq C|x - x_0|^n.$$

Since f is analytic n exists for all orders, $h(x_0) = \infty$ as needed. □

Corollary 2.1.6. e^x has $h(x_0) = \infty$ for any point $x_0 \in \mathbb{R}$.

Proof. Since e^x is an analytic function we use Proposition 2.1.5 as needed. □

These h values give a notion of the strength of the singularity which is illustrated below, for $f(x) = |x-5|^h$ where h takes the following values $0.1, 0.3, 0.5, 0.7$. Notice in Figure 2.1 that as h increases the weaker the singularity becomes at $x = 5$ while lower h values correspond to a stronger singularity. In the following section we shall see a function that has the same Hölder exponent everywhere, which is characterized by the Hurst exponent.

2.2 Hurst Exponent and Fractional Brownian Motion (fBm)

In the previous section we saw how the Hölder exponent quantifies the strength of a local singularity. Now consider a signal that is continuous everywhere, but nowhere differentiable

that has the same Hölder exponent everywhere, that is, for all x_0 in the domain, $h(x_0)$ remains constant. This is characterized by the Hurst exponent H, a single exponent that describes the roughness of the signal. The Hurst exponent is not a function of space or time, that each point has the same singularity strength.

Fractional Brownian motions (fBm) are processes that are governed by the Hurst exponent, they have homogeneous roughness. These processes are used throughout many scientific disciplines. To alleviate the text and for simplicity, the introduction and explorations of notions surrounding fBms was kept to 1D even though the analyses of subsequent chapters make use of 2D fBms.

Definition 2.2.1 (fractional Brownian motion (fBm))**.** From [9, 21, 29], a fractional Brownian motion of Hurst exponent $0 < H < 1$ is a Gaussian process $B_H(t)$ such that

$$B_H(0) = 0 \text{ and } B_H \text{ is continuous}$$

and for every $t \geq 0$ and $b > 0$ the increment $B_H(t+b) - B_H(t)$ follows the normal distribution with mean zero and variance b^{2H} so that

$$P(B_H(t+b) - B_H(t) \leq s) = \frac{1}{b^H\sqrt{2\pi}} \int_{-\infty}^{s} \exp\left(\frac{-x^2}{2b^{2H}}\right) dx. \tag{2.5}$$

We will verify the mean and variance in Eq. (2.5).

Lemma 2.2.1. With the terms defined in Eq. 2.5, the following holds

$$\int x \exp\left(\frac{-x^2}{2b^{2H}}\right) dx = -b^{2H} \exp\left(\frac{-x^2}{2b^{2H}}\right) + C.$$

Proof. With $u = \frac{-x^2}{2b^{2H}}$ consider the following,

$$\begin{aligned}\int x \exp\left(\frac{-x^2}{2b^{2H}}\right) dx &= -b^{2H} \int e^u du = -b^{2H} e^u + C \\ &= -b^{2H} \exp\left(\frac{-x^2}{2b^{2H}}\right) + C\end{aligned}$$

as needed. □

Proposition 2.2.2. The mean of the probability density function in Eq. (2.5) is 0.

Proof. By Eq. (2.5) we have,

$$E\left(B_H(t+b) - B_H(t)\right) = \frac{1}{b^H\sqrt{2\pi}} \int_{-\infty}^{\infty} x \exp\left(\frac{-x^2}{2b^{2H}}\right) dx$$

by Lemma 2.2.1,

$$\frac{-b^H}{\sqrt{2\pi}} \int_{-\infty}^{-\infty} e^u du = \frac{-b^H}{\sqrt{2\pi}} e^u \Big|_{-\infty}^{-\infty} = 0$$

as needed. □

Proposition 2.2.3. The variance of the probability density function in Eq. (2.5) is b^{2H}.

Proof. From [6] we know that for a random variable Y,

$$Var(Y) = E(Y^2) - \left(E(Y)\right)^2.$$

From the previous Proposition 2.2.2 we know that

$$E\left(B_H(t+b) - B_H(t)\right) = 0$$

and therefore

$$Var\left(B_H(t+b) - B_H(t)\right) = E\left(\left(B_H(t+b) - B_H(t)\right)^2\right).$$

Now consider that

$$E\left(\left(B_H(t+b) - B_H(t)\right)^2\right) = \frac{1}{b^H\sqrt{2\pi}} \int_{-\infty}^{\infty} x^2 \exp\left(\frac{-x^2}{2b^{2H}}\right) dx.$$

We proceed with integration by parts with $u = x$ and $v = -b^{2H} \exp\left(\frac{-x^2}{2b^{2H}}\right)$ by Lemma 2.2.1. Now the integral becomes

$$\frac{1}{b^H\sqrt{2\pi}} \left(-xb^{2H} \exp\left(\frac{-x^2}{2b^{2H}}\right) \Big|_{-\infty}^{\infty} + \int_{-\infty}^{\infty} b^{2H} \exp\left(\frac{-x^2}{2b^{2H}}\right)\right)$$

$$= \frac{2b^{2H}}{b^H\sqrt{2\pi}} \int_0^{\infty} \exp\left(\frac{-x^2}{2b^{2H}}\right) dx.$$

Now by a change of variable $y = \frac{x^2}{2b^{2H}}$ and $dx = \frac{b^{2H}}{x}dy$

$$\frac{2b^{2H}}{\sqrt{2\pi}} \int_0^\infty \frac{b^{2H}}{x} e^{-y} dy$$

note that $x = \sqrt{y2b^{2H}}$ therefore

$$\frac{2b^{3H}}{\sqrt{2\pi}} \int_0^\infty \frac{1}{\sqrt{y2b^{2H}}} e^{-y} dy = \frac{b^{2H}}{\sqrt{\pi}} \int_0^\infty y^{-1/2} e^{-y} dy$$

by the gamma function [6], we have

$$= \frac{b^{2H}}{\sqrt{\pi}} \Gamma(\frac{1}{2}) = b^{2H}$$

as needed. □

We will prove the covariance of an fBm, which will illustrate the statistical tendencies mentioned earlier. These next propositions are useful in proving the covariance.

Proposition 2.2.4. $E((B_H(t))^2) = t^{2H}$.

Proof. See [23]. □

Proposition 2.2.5. $E(B_H(t)B_H(t+b)) = \frac{1}{2}(t^{2H} + (t+b)^{2H} - b^{2H})$.

Proof. From Eq. 2.5 we know that,

$$E\left((B_H(t+b) - B_H)^2\right) = b^{2H}$$

$$E\left((B_H(t+b) - B_H)(B_H(t+b) - B_H)\right) = b^{2H}$$

$$E\left((B_H(t+b))^2 - 2B_H(t)B_H(t+b) + (B_H(t))^2\right) = b^{2H}$$

$$E((B_H(t+b))^2) - 2E(B_H(t)B_H(t+b)) + E((B_H(t))^2) = b^{2H}$$

$$-2E(B_H(t)B_H(t+b)) = b^{2H} - E((B_H(t+b))^2) - E((B_H(t))^2)$$

from Proposition 2.2.4 we have

$$E(B_H(t)B_H(t+b) = \frac{1}{2}\left(t^{2H} + (t+b)^{2H} - b^{2H}\right)$$

as needed. □

Proposition 2.2.6. $E\left((B_H(t) - B_H(0))(B_H(t+b) - B_H(t)\right) = \frac{1}{2}\left((t+b)^{2H} - t^{2H} - b^{2H}\right).$

Proof. We have, by Eq. 2.5

$$E\left((B_H(t) - B_H(0))(B_H(t+b) - B_H(t)\right) = E\left(B_H(t)(B_H(t+b) - B_H(t)\right)$$

$$= E\left(B_H(t)B_H(t+b) - (B_H(t))^2\right) = E(B_H(t)B_H(t+b)) - E((B_H(t))^2)$$

by Proposition 2.2.4 and 2.2.5,

$$= \frac{1}{2}(t^{2H} + (t+b)^{2H} - b^{2H}) - t^{2H} = \frac{1}{2}((t+b)^{2H} - t^{2H} - b^{2H})$$

as needed. □

From Proposition 2.2.6, we see that $H = 1/2$ gives a zero covariance which means that the increments are independent. Furthermore, $H = 1/2$ is Brownian Motion which is associated with coin flip randomness. For $0 < H < 1/2$ the covariance is negative which corresponds to anti-persistence, while $1/2 < H < 1$ gives a positive covariance for long-range correlation statistical tendencies [2, 9, 29]. Additionally, the probability density function in Definition 2.5 does not depend on t and so the increments are stationary for all H. In Figure 2.2, inspired by [29], we see that different Hurst exponents correspond to different roughness behavior in the signal.

Falconer [9] showed that for $\lambda \in \mathbb{R}$, $H \in (0, 1)$, $0 < \lambda < H$ then with probability 1 there is a constant $K \in \mathbb{R}$ such that

$$|B_H(t+b) - B_H(t)| \leq K|H|^{\lambda}.$$

Note that the $\sup \lambda = H$ since λ cannot be equal to H, the largest possible value. In other words fBms are of homogeneous roughness satisfying the requirement for the Hurst Exponent [9]. This is why one can say that fBms are governed by the Hurst exponent.

From Figure 2.2 the following terms make intuitive sense.

This is directly related to the singularity behavior shown in Figure 2.1. For instance, $f(x) = |x - 5|^{0.7}$ has a singularity at $x = 5$ with $h = 0.7$ but for the Hurst exponent (H) now every point has the same roughness, the same singularity everywhere rather than isolated singularities. This marks the distinction between h and H, where h is a function of either time or space while H is independent of time or space, the roughness is homogeneous. This notion of roughness is intimately related with the Fractal Dimension, as demonstrated in the following section; the instances of fBms are all monofractals.

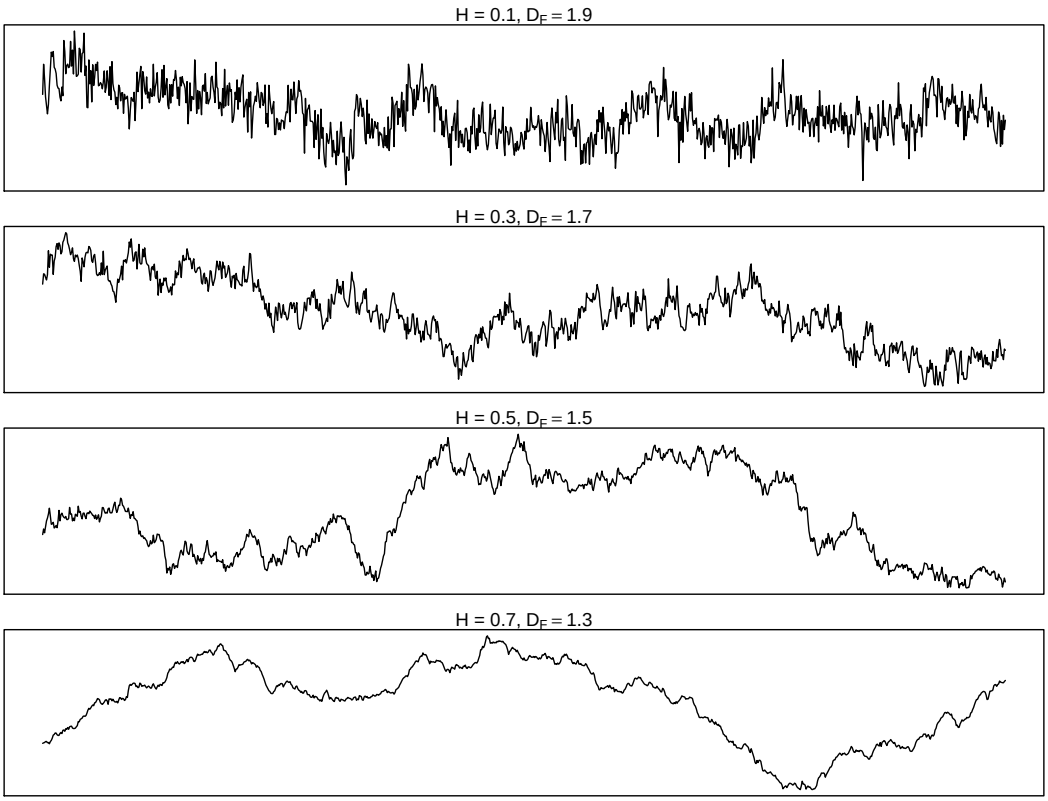

Figure 2.2: This figure highlights the different behavior of 1D fBms as a function of the Hurst exponent. The larger the H the more smooth the fBm and the lower the fractal dimension.

2.3 Fractal Dimension

Fractal phenomena are present in many different fields. Fractal geometry was originally developed by Mandelbrot to explore patterns in natural phenomena that did not adhere to Euclidean geometry. For instance, a classic example is the coast line of Britain [22] which

upon magnification reveals more coastline which resembles the original coastline. This is a critical idea of fractals, called self-similarity which can be either exact or statistical. Loosely speaking self-similarity means that the signal behaves (looks) the same at every level of magnification. The fractal dimension is a generalized notion of the Euclidean dimension that allows for noninteger dimensions. The fractal dimension D_F gives a measure of how much space a fractal occupies. An example of a fractal is displayed in Figure 2.3.

Fractional Brownian motions are self-similar [21, 29] and the fractal dimension for a 1D fBm is given by $D_F = 2 - H$ [22] and [1]. For $H = 0.1$, $D_F = 1.9$ which means that the fractal nearly occupies as much space as a 2D object. Another perspective on viewing fBms is also illustrated in Figure 2.2, where the lower H values are more rough which means that they occupy more space. The larger H values have D_F closer to one and more approximate a line, they are more smooth. Furthermore, D_F quantifies a large class of functions. Some of these functions can be made to fit $D_F = 2 - H$, for instance the Koch Curve displayed in Figure 2.3. It is possible to make the Koch Curve resemble a fBm by cutting through the center horizontally and bringing up the bottom half to make a 1D "time-series." The fractal dimension is still 1.26 but now we can use $D_F = 2 - H$ to get $H \approx 0.74$

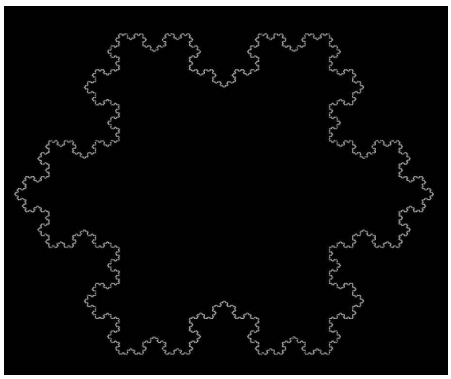

Figure 2.3: The Koch curve has $D_F = \frac{\log(4)}{\log(3)} \sim 1.26$ [14]. The fractal dimension is a generalized notion of dimension that includes Euclidean dimension. It is a measurement of how much space a fractal occupies.

A common way to estimate D_F is with the the Box-Counting dimension [3].

Definition 2.3.1 (Box-Counting Dimension)**.** The Box-Counting Dimension is defined as, if the limit exists,

$$D = \lim_{n\to\infty} \frac{\log N_n}{\log \frac{1}{S_n}}$$

where N_n is the number of boxes of size S_n required to cover the fractal, a compact set, at the n-th iteration.

Note that this is only one method to estimate D_F and keep in mind that the fractal only exists as $n \to \infty$. There are different ways to generate fractals that are not fBms [3], but this is beyond the scope of this paper. A classic example of a fractal, that is not a fBm, is the Cantor Set which is generated by consecutively removing the middle third ad infitium of a closed line segment usually $[0, 1]$. Note that $D_F = 2 - H$ does not apply to the Cantor set because it is not continuous, nonetheless the D_F can still be obtained by the Box Counting Dimension.

Definition 2.3.2 (Cantor Set)**.** Let $C_0 = [0, 1]$ and $C_n = \frac{C_{n-1}}{3} \cup \left(\frac{2}{3} + \frac{C_{n-1}}{3}\right)$ for $n \geq 1$. Then the Cantor Set is $C = \cap_{n=0}^{\infty} C_n$

The first few iterations of the Cantor Set are displayed in Figure 2.4, keep in mind the iterations are not actually the Cantor Set, which only exists when $n = \infty$. This is an example of an exact self-similar fractal because at every iteration the generation procedure is exactly the same. Moreover at any iteration, $n \geq 1$, for $a = 3^n$ one can take a single component of C_n, shift the interval so it starts at zero and then multiply the interval by a, returning C_0, thus showing a scale-invariant property.

Proposition 2.3.1. The Box-Counting dimension of the Cantor Set is log(2)/log(3).

Proof. Note that $N_n = 2^n$ and $S_n = \frac{1}{3^n}$ since for every iteration there are 2^n segments of length $\frac{1}{3^n}$. Furthermore observe that

$$\log \frac{1}{\frac{1}{3^n}} = \log 3^n = n \log 3.$$

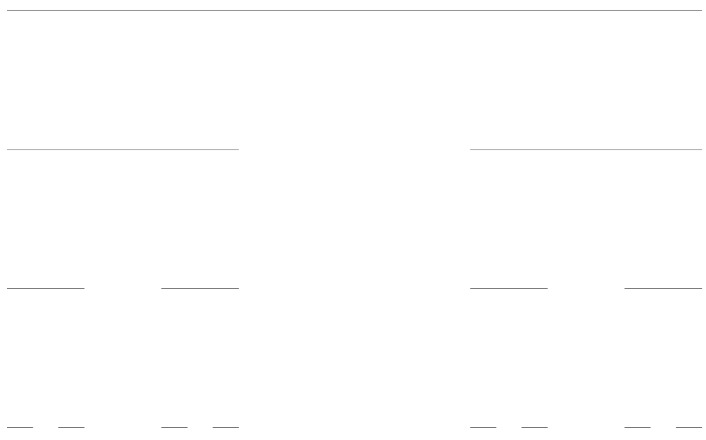

Figure 2.4: First few iterations of generating the Cantor set by the deterministic algorithm [3].

By Definition 2.3.1 we have

$$D = \lim_{n\to\infty} \frac{\log N_n}{\log \frac{1}{S_n}} = \lim_{n\to\infty} \frac{\log 2^n}{\log \frac{1}{\frac{1}{3^n}}}$$

$$= \lim_{n\to\infty} \frac{\log 2^n}{\log 3^n} = \lim_{n\to\infty} \frac{n \log 2}{n \log 3} = \frac{\log 2}{\log 3} \approx 0.6309.$$

□

Compare this to the Box Counting dimension of a line on $[0, 1]$, which at every iteration requires one box of length 1. Definition 2.3.1 becomes

$$D = \lim_{n\to\infty} \frac{\log N_n}{\log \frac{1}{S_n}} = \lim_{n\to\infty} \frac{1}{\log \frac{1}{\frac{1}{1}}} = 1$$

which conforms with the Euclidean Dimension. As mentioned earlier, the fractal dimension is a generalized notion of the Euclidean dimension that allows for noninteger dimensions and it gives a measure of how much space a fractal occupies. Intuitively this makes sense with our example; the Cantor Set has a dimension less than the line but is not zero because the Cantor Set is not just a single point, with a point having $D = 0$. Furthermore, strong support for the Box-counting Dimension comes from Analysis. These boxes are actually balls and a fractal, in this context, is a compact set.

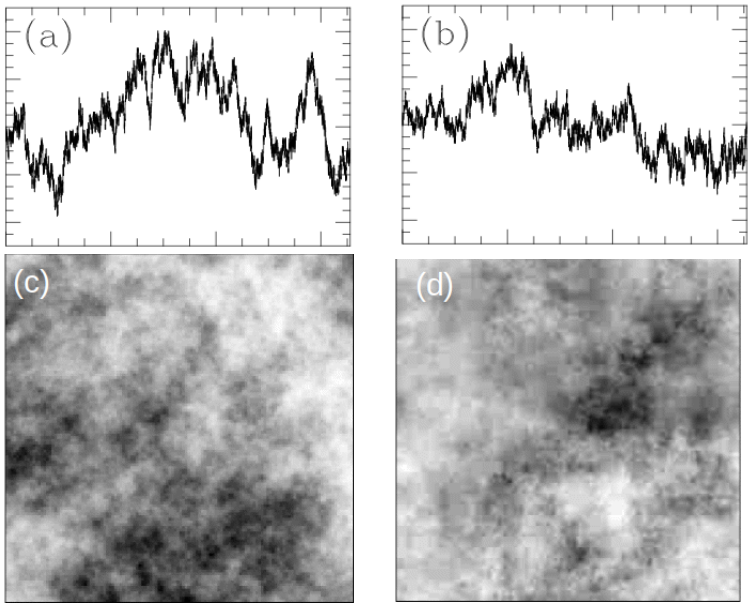

Figure 2.5: From [2, 7] (a) is a monofractal signal with $H = 1/3$. (b) is multifractal signal with roughness exponents ranging from $h = 0.155$ to $h = 0.555$. (c) is a 2D fractional Brownian motion with $H = 1/2$. (d) is a 2D multifractal, with a spectrum of roughness exponents ranging from $h = 0.1$ to $h = 0.6$.

2.3.1 Multifractals and Roughness Exponents

A *multifractal* signal has heterogeneous roughness while a *monofractal* signal has homogeneous roughness. To summarize, a very important point is that, a multifractal has multiple roughness exponents that describe the signal while a monofractal has a single roughness exponent that describes the signal. In other words, a multifractal is described by a spectrum of Hölder exponents while a monofractal is described by the Hurst exponent. The difference between a monofractal and a multifractal is not obvious as in Figure 2.5 borrowed from [7].

The difference is very important because other popular methodologies, including Fourier Power Spectrum assume an underlying monofractal signal. These methodologies will output an incorrect measurement for the roughness if a multifractal is analyzed. Worse, they can not discriminate monofractal and multifractal signals; they will only output a single roughness exponent even when the underlying signal has a spectrum of roughness exponents. Figure 2.5 illustrates that the difference is not immediately obvious.

2.4 2D Wavelet Transform Modulus Maxima Method

The 2D Wavelet Transform Modulus Maxima (WTMM) method is the multifractal methodology the lab's algorithm utilizes, it is built upon the Continuous Wavelet Transform (CWT). This section starts with the CWT and then moves on to the 2D WTMM method. Throughout this section, the notation, terminology and definitions come from [2].

The CWT allows the ability to analyze frequencies that are localized by time or space. This permits the investigation into local phenomena of the signal. In comparison, the Fourier Transform only allows for global analysis. The power spectrum analysis can not localize salient features of the signal. The result of the CWT are wavelet coefficients which are a function of scale (inverse relationship with frequency) and a space parameter.

Definition 2.4.1. The CWT coefficients are defined as,

$$\mathbf{T}_{\psi}[f](\mathbf{b}, a) = \begin{pmatrix} T_{\psi_1}[f] = a^{-2} \int \psi_1(a^{-1}(\mathbf{x} - \mathbf{b}))f(\mathbf{x})d^2\mathbf{x} \\ T_{\psi_2}[f] = a^{-2} \int \psi_2(a^{-1}(\mathbf{x} - \mathbf{b}))f(\mathbf{x})d^2\mathbf{x} \end{pmatrix}$$

where $\mathbf{b}$ is the space parameter, $f \in L^2(\mathbb{R})$ is, a represents scale, $\mathbf{x} = (x, y)$ and ψ is the wavelet.

For this research we used the Gaussian function $\mathcal{G}(x, y)$, and defined the wavelets as:

$$\psi_1(x, y) = \frac{\partial \mathcal{G}(x, y)}{\partial x} \text{ and } \psi_2(x, y) = \frac{\partial \mathcal{G}(x, y)}{\partial y}$$

where

$$\mathcal{G}(x, y) = e^{-(x^2+y^2)/2} = e^{-|\mathbf{x}|^2/2}$$

An additional property of the Gaussian wavelets is that they are orthogonal to lower order polynomials [2]. This is useful in singularity detection since a Taylor Polynomial is utilized in the definition of the Hölder exponent as explained in Section 1.1. The first order Gaussian wavelet, utilized in this research, is orthogonal to constant behavior in the signal,

that this they integrate to zero when multiplied by a constant. Recall, that the class of functions we are interested in do not have a Taylor Polynomial beyond the function value. The following proposition shows that the first derivative Gaussian wavelet is orthogonal to constant behavior.

Proposition 2.4.1. The first derivative Gaussian wavelet $\psi_1(x, y)$ and $\psi_2(x, y)$ is orthogonal to constant behavior.

Proof. Without a loss of generality, the proposition will be shown for $\psi_1(x, y)$, for $Z \in \mathbb{R}$ with $Z > 0$,

$$\begin{aligned}\int_{-\infty}^{\infty}\int_{-\infty}^{\infty} Z\psi_1(x,y)dxdy &= Z\int_{-\infty}^{\infty}\int_{-\infty}^{\infty} -xe^{-(x^2+y^2)/2}dxdy \\ &= Z\int_{-\infty}^{\infty} e^{-y^2/2}dy\int_{-\infty}^{\infty} -xe^{-x^2/2}dx\end{aligned}$$

where $u = \frac{-x^2}{2}$ giving both integral bounds as $-\infty$,

$$= Z\int_{-\infty}^{\infty} e^{-y^2/2}dy\int_{-\infty}^{-\infty} e^{u}du = 0$$

as needed. □

Proposition 2.4.1 can be generalized such that order $n+1$ derivative Gaussian wavelets are orthogonal to polynomials of degree n [1, 2, 21]. Although this property was not utilized, it is worth mentioning.

The wavelet transform can be expressed in polar coordinates, i.e. in terms of its modulus and argument:

$$\mathbf{T}_\psi[f](\mathbf{b}, a) = (\mathcal{M}_\psi[f](\mathbf{b}, a), \mathcal{A}_\psi[f](\mathbf{b}, a))$$

where

$$\mathcal{M}_\psi[f](\mathbf{b}, a) = \left((T_{\psi_1}[f](\mathbf{b}, a))^2 + (T_{\psi_2}[f](\mathbf{b}, a))^2\right)^{0.5}$$

$$\mathcal{A}_\psi[f](\mathbf{b}, a) = Arg\left(T_{\psi_1}[f](\mathbf{b}, a) + iT_{\psi_2}[f](\mathbf{b}, a)\right).$$

$\mathcal{M}_\psi[f](\mathbf{b}, a)$ is the modulus of the wavelet transform while $\mathcal{A}_\psi[f](\mathbf{b}, a)$ is the argument.

The WTMM are locations $\mathbf{b}$ where $\mathcal{M}_\psi[f](\mathbf{b}, a)$ is a local maximum in the direction of $\mathcal{A}_\psi[f](\mathbf{b}, a)$ for a given scale a. The WTMM capture the gradient changes in the underlying signal. The WTMM are on connected chains, called maxima chains [2]. This process is repeated at every scale and an example for a 2D fBm with $H = 0.7$ is provided in Figure 2.6a, the black lines are the WTMM.

The WTMM maxima (WTMMM) are defined as the points along the maxima chains where $\mathcal{M}_\psi[f](\mathbf{b}, a)$ is locally maximum. The WTMMM are connected through scales, a, and these connected WTMMM are called maxima lines. The maxima lines are formed by linking the WTMMM with the nearest WTMMM at the next scale. The set of all maxima lines is called the WT skeleton and illustrated in Figure 2.6b. The Wavelet Transform (WT) Skeleton contains the spatial information about the maxima lines, each point in Figure 2.6b contains (x, y, a) coordinates and the value of the WTMMM at that point. The following power laws remove the need for the spatial information with maxima curves [2].

Remark. The WTMMM follow,

$$\mathcal{M}_\psi[f](\mathcal{L}_{\mathbf{x_0}}(a)) \sim a^{h(\mathbf{x_0})}$$

as $a \to 0^+$ where $\mathcal{L}_{\mathbf{x_0}}(a)$ is the maxima line at $\mathbf{x_0}$, and $h(\mathbf{x_0})$ is the roughness exponent. See [1] and references therein for a detailed explanation.

For reference, $\mathcal{L}_{\mathbf{x_0}}(a)$ is the maxima line from Figure 2.6b for some point $\mathbf{x_0}$. From Definition 2.4, a log-log plot will estimate the roughness exponent $h(\mathbf{x_0})$ by following the behavior of the maxima line through the scales a

$$\frac{\log(\mathcal{M}_\psi[f](\mathcal{L}_{\mathbf{x_0}}(a)))}{\log(a)} \sim h(\mathbf{x_0}).$$

Figure 2.6c shows such a log-log plot and is named a sheaf (sheaves). To reiterate an important point, Definition 2.4 permits the estimation of the roughness exponent from the sheaf in Figure 2.6c. To clarify, Figure 2.6c and Figure 2.6b both contain the same maxima

lines however, Figure 2.6b preserves the spatial information. The data from the sheaf, Figure 2.6c is passed to the partition functions.

2.4.1 Partition Function and Statistical Order Moments

Statistical order moments (q values) play a crucial role in the 2D WTMM method. These values allow one to emphasize different singularity strengths of the underlying signal by weighting the modulus of the wavelet transform along the maxima lines. The quantity and quality of the underlying data will determine the range of the available statistical order moments. A wide range of statistical order moments allows for a more detailed picture of the underlying signal.

Definition 2.4.2. Let $\mathcal{L}(a)$ be the set of maxima lines at scale a and define the *partition function* as:

$$Z(q,a) = \sum_{l \in \mathcal{L}(a)} \left(\sup_{(\mathbf{b},a') \in l, a' \leq a} \mathcal{M}_\psi[f](\mathbf{b},a') \right)^q$$

where q are the statistical order moments.

A power-law relationship was defined for the partition function in [2]. Note that negative q values give more weight to small modulus values while positive q values give more weight to large modulus values. This power-law is what allows us to get an estimate for the roughness for a signal.

Remark. The power-law of the partition function is,

$$Z(q,a) \sim a^{\tau(q)}, a \to 0^+.$$

See [1] and references therein for a detailed explanation.

From a log-log plot it is possible to obtain an estimate for $\tau(q)$. For a mathematically rigorous development of the partition function and $\tau(q)$ see [9, 13] and [1] and references therein. In the case of a monofractal, $\tau(q)$ is a linear function where the slope of $\tau(q)$ gives

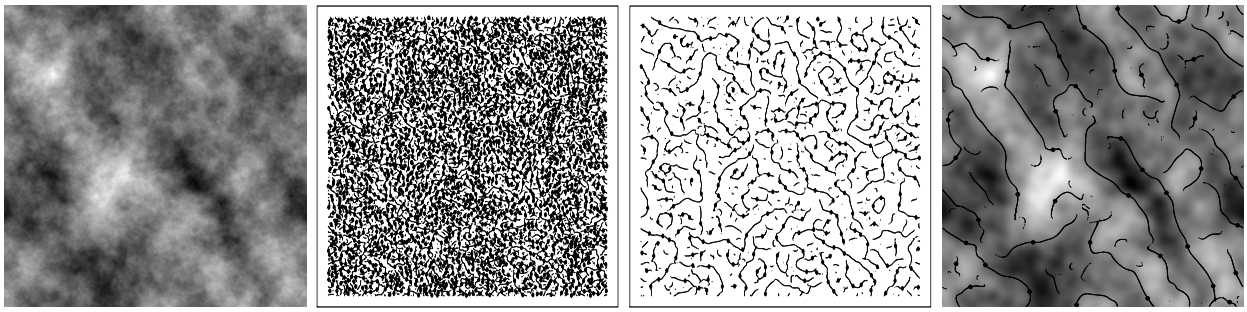

Figure 2.6a: The left most diagram is a fractional Brownian surface with $H = 0.7$, following the maxima chains for $a = 15$ (19.8 pixels), then $a = 30$ (56 pixels), and the last right diagram is an overlay of the WTMM and WTMMM on the original image smoothed at scale $a = 45$ (158 pixels). The methodology preserves spatial information and captures the gradient changes. The larger the scale the less detail. The black lines are the WTMM while the black dots are the WTMMM.

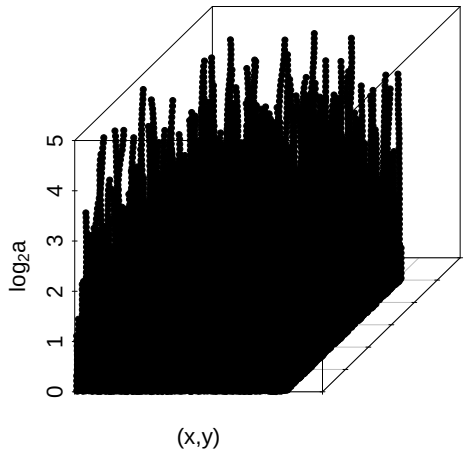

Figure 2.6b: Each line is known as a maxima line. They are the WTMMM connected through scales, by linking the WTMMM closest at the next scale. The position in the original image is preserved, the x and y coordinates are for the underlying signal.

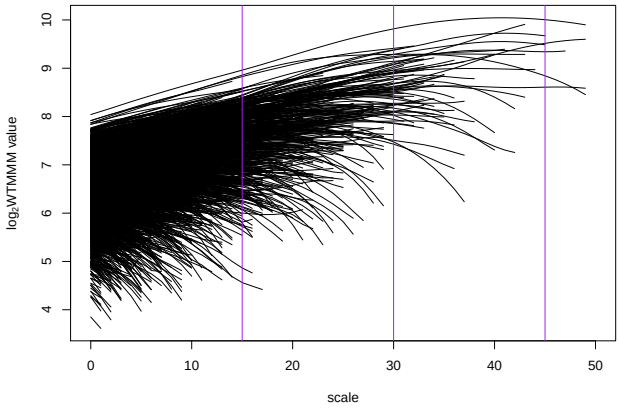

Figure 2.6c: The three vertical purple lines correspond to $15, 30, 45$ the scales represented in Figure 2.6a. The black dots in Figure 2.6a are connected through all the scales to generate this figure, known as a sheaf.

Figure 2.6: This is an example of the 2D WTMM method with generating the maxima lines for a fractional Brownian surface with $H = 0.7$.

an estimate for the Hurst exponent. However in a multifractal, $\tau(q)$ is nonlinear which highlights the varying roughness exponents in the underlying signal.

The reason for a discrete sum instead of an integral is to prevent singularities for negative q values. Additionally, the 2D WTMM method includes something similar to the box counting method, where $\tau(0)$ gives box counting method except that instead of boxes, small oscillating functions (wavelets) are utilized [2]. This can be seen in Definition 2.4.2 with a 0 for an exponent and the sum counting the maxima lines at a given scale. Furthermore, $\tau(2)$ is related to power spectrum analysis with $\beta = 2 + \tau(2)$ where β is the scaling exponent of the spectral density [2].

In addition to $\tau(q)$ there are expectation values, that utilize the partition function, which give estimates for the dimension and the roughness. These expectation values are used since using the Legendre transform involves smoothing $\tau(q)$ which could mask non-analytic curves [2].

Definition 2.4.3. From [2] let,

$$W_\psi[f](q,l,a) = \frac{\left|\sup_{(\mathbf{b},a')\in l, a'\leq a} \mathcal{M}_\psi[f](\mathbf{b},a')\right|^q}{Z(q,a)}$$

$$h(q,a) = \sum_{l\in\mathcal{L}(a)} \ln\left|\sup_{(\mathbf{b},a')\in l, a'\leq a} \mathcal{M}_\psi[f](\mathbf{b},a')\right| W_\psi[f](q,l,a)$$

$$D(q,a) = \sum_{l\in\mathcal{L}(a)} W_\psi[f](q,l,a)\ln W_\psi[f](q,l,a)$$

This gives the following,

$$h(q) = \frac{d\tau(q)}{dq} = \lim_{a\to 0^+} \frac{h(q,a)}{\ln a}$$

$$D(q) = \lim_{a\to 0^+} \frac{D(q,a)}{\ln a}.$$

In order to have proper statistics the curves in $D(a,q)$ and $h(a,q)$ need to follow power law behavior in order to be included in the $D(q)$ and $h(q)$ functions.

Definition 2.4.4. From [2], let f be a function from $\mathbb{R}^2$ into $\mathbb{R}$ and S_h the set of all points x_0 so that the Hölder exponent of f at x_0 is h. The singularity spectrum $D(h)$ of f is the function which associates with any h, the fractal dimension of S_h

$$D(h) = D_F\{\mathbf{x} \in \mathbb{R}^2 \ , \ h(\mathbf{x}) = h\}.$$

Definition 2.4.4 defines a singularity spectrum of all the various h values a function may contain. Here $h(x)$ is a function and h is a particular value, the notation comes from the literature. Observe, that in a monofractal $D(h)$ collapses to a single point because the roughness is homogeneous. While a multifractal function will have an upside down parabola whose width corresponds to the extent of the variety of roughness exponents characterizing the signal [1]. From $D(h)$ one can find the most predominant roughness exponents for a multifractal. To clarify, D corresponds to the dimension and h corresponds to the roughness exponent(s) and Definition 2.4.3 gives that $D(h)$ is $D(h(q))$. An example of this process is given in the following section.

CHAPTER 3

THE DEVELOPMENT OF THE RESCUE METHOD FOR SATURATED IMAGES

For an experimental environment, we generated 32 fractional Brownian surfaces of size 1024x1024 for $H = 0.1, 0.3, 0.5, 0.7$. The number 32 comes from [1] which says that 32 is an appropriate amount to get a "quintessential" statistical results from a fractional Brownian surface. Recall that they are statistical processes and hence single instances can deviate from the "expected" path. Thus all the figures and statistics in this section are averages of the individual statistical results of the 32 fractional Brownian surfaces. We also saturated the images at the 1%, 5%, 10% and 20% levels. This chapter begins by applying the 2D WTMM method for all the fBm surfaces without saturation, then looking at the effects of image saturation on $h(a, q)$ and $D(a, q)$, described in Definition 2.4.3, and the resulting loss of statistical order moments. Then we explain the development of the rescue method, we illustrate the iterative process of creating the novel technique by analyzing sheaves. The rescue method is then applied to saturated images as a means of recapturing some lost statistical order moments.

We are utilizing fBms to mimic the output statistics from an actual mammogram. The methodology is the same for both, however we have numerical control over the fBms.

3.1 Detailed Overview of the 2D WTMM Method on Fractional Brownian Motion Surfaces

Previous research has illustrated the efficacy of the 2D WTMM method with fBm surfaces [1, 2]. Furthermore, the 2D WTMM method works in a similar way for different fBm surfaces and in order to alleviate the text, we will focus on $H = 0.7$.

In Figure 3.1, one can see equations from Definition 2.4.3 for unsaturated fBm surfaces. Note that in Figure 3.1a and 3.1b the curves are all averages of the individual analyses of the 32 fractional Brownian motions surfaces with $H = 0.7$. Additionally note how both figures have curves with a relatively good power law fit for the statistical order moments. Recall that these figures are generated by weighting the maxima lines from Figure 2.6c with a range of q values from $-3 \leq q \leq 5$ with negative q values weighting small values of the modulus more and larger q values weighting larger values of the modulus more. Observe that the black curves are shifted down versions of $q = 0$ for illustrative purposes only, this is the benchmark of a good power law fit. This benchmark curve also highlights the range of scales used from 0.1 to 3.75. Although, there is not image saturation present, at scales larger than 3.75, especially in Figure 3.1a one can see the linearity diminished. This nonlinear behavior is a numerical effect because of the underlying size of the images. If we used larger images these curves would become more straight for a larger range of scales, and we could include more statistical order moments. However, with image saturation in the next section, this range is greatly impacted for the same set of images.

From Figures 3.1a and 3.1b we generate Figures 3.1c and 3.1e which include the values for the other Hurst exponents. Both are generated by taking the slope of each curve in Figure 3.1a and 3.1b, which highlights the importance of linearity in the trends. It is not proper to get a power law fit for a nonlinear trend. Each point in Figure 3.1c on the curve near 0.6 is the slope of the corresponding statistical order moment in 3.1a as described in Definition 2.4.3. To clarify, the other curves displayed in Figures 3.1c and 3.1e correspond to other Hurst exponents in which they each have their own $h(a, q)$ and $D(a, q)$ plots which are the averages of 32 fBm's with respective Hurst exponents.

In the $D(q)$ plot in Figure 3.1, one can see that the 2D WTMM method provides consistent estimates for the dimension of the image. That regardless of the q values used in the range kept, we get an estimate for the dimension around 2. The estimate for H comes from

taking the slope of best fit yet again on the $h(q)$ plot in Figure 3.1. Note that although the methodology consistently underestimates the actual Hurst exponent, the estimates are consistent which is of main importance. Furthermore the error is not relative but rather absolute since we are estimating an exponent. Figure 3.1f shows the $D(h)$ plot as described in Definition 2.4.4, most of the points are clustered near 2. This is correct because the dimension of an image is 2 and the roughness throughout the image has an exponent of $H = 0.7$. The $D(h)$ plot is confirming that the fBm surface is indeed a monofractal with a roughness exponent $H = 0.7$.

3.2 Overview of Saturated fBm Surfaces with $H = 0.7$

In this section we look at the fBm surfaces with $H = 0.7$ and saturation at the 20%, 10%, 5% and 1% levels. This is without a loss of generality since, the other fractional Brownian motion surfaces experienced similar effects in the 2D WTMM statistics.

Figure 3.2 shows a fBm process with $H = 0.7$ saturated and the resulting sheaves, as defined in the previous chapter. There is a distinct difference from Figure 3.2a and Figures 3.2b, 3.2c, 3.2d and 3.2e, namely the low modulus values that exist in all saturation levels. These low modulus values highlight the lack of gradient changes within the image. Intuitively, this makes sense, as these fBms are long-range correlated and the saturation is occurring at the 80% percentile or higher. As mentioned earlier, these saturated islands are most predominate for this H value. Figures 3.2b, 3.2c, 3.2d and 3.2e are passed to the expectation functions in order to generate $h(a, q)$ and $D(a, q)$.

Figure 3.3 conveys the impact of image saturation on the statistics from the 2D WTMM method. Similarly to the sheaves, an immediate difference is observable relative to unsaturated fBm surfaces. In Figures 3.3a, 3.3b, 3.3c and 3.3d one can see stair step behavior in the $h(a, q)$ curves that did not exist in the unsaturated case as in Figure 3.1. It is not proper to take a slope of best fit for those curves, and thus those statistical order

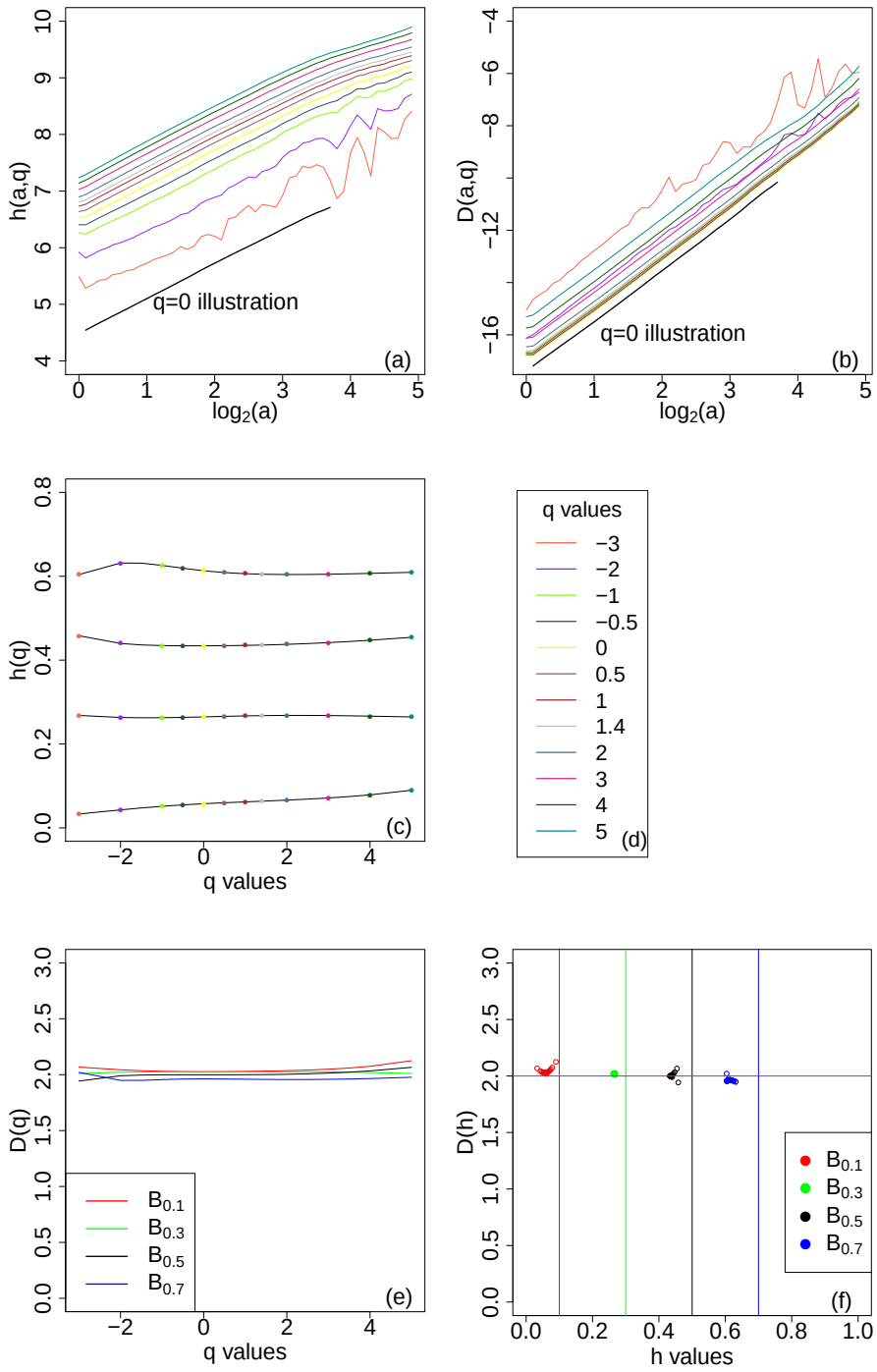

Figure 3.1: We take the best fit slope of each curve (unique q value) in (a) and (b) and plot the value in (c) and (e). (d) is the legend for the q values. Note the straight curves and the consistent estimates, regardless of statistical order moment. This is the process for estimating the roughness exponent and dimension for a monofractal for different statistical order moments. Note that $q = 0$ is shifted down for display purposes, this is the benchmark for a good power law fit. (e) confirms the monofractal image with a consistent dimension of 2 for all the roughness exponents. (f) is the $D(h)$ plot with vertical lines at the Hurst exponent which these fBm surfaces were generated. For each set of fBms the statistics are consistent with a monofractal image.

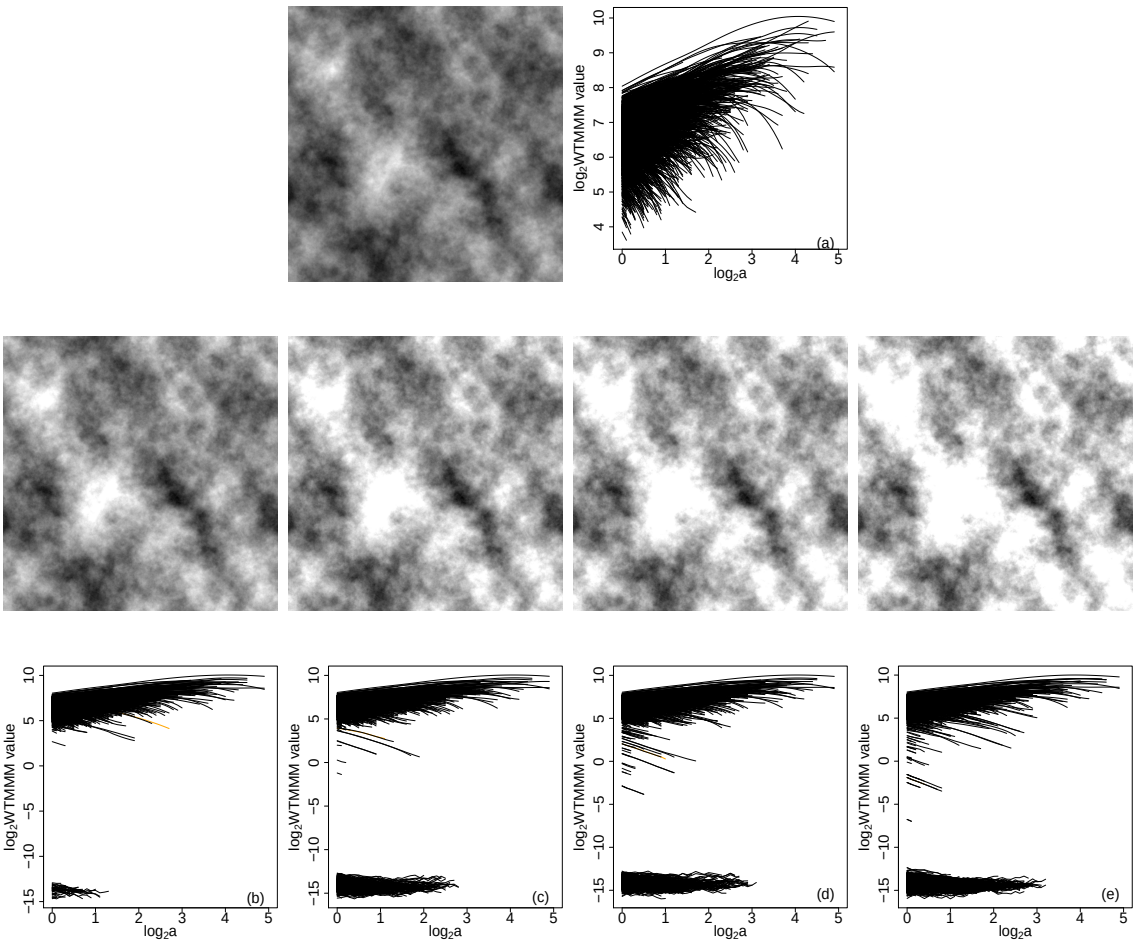

Figure 3.2: (a) The sheaf for the fractional Brownian motion surface with $H = 0.7$ pictured left. $(b) - (e)$ The corresponding sheafs to the above fractional Brownian surfaces, saturated at 1%, 5%, 10% and 20% from left to right. Notice the extremely low modulus values for the saturation levels. These maxima lines are those that will interfere with $h(a, q)$ and $D(a, q)$ plots, which then reduces the number of statistical order moments as shown Figure 3.3.

moments are removed from the analysis and hence the next set of plots, Figures 3.3e, 3.3f, 3.3g and 3.3h, are missing statistical order moments (black dots) compared to the unsaturated case (blue dots). For reference $-3 \leq q < -0.10$ were eliminated. A narrower range of statistical order is a concern for the mammogram analysis, we have less statistics for a given subregion. A wider range of q values, as discussed in the previous section, allows the implementer to emphasize various underlying aspects of the signal.

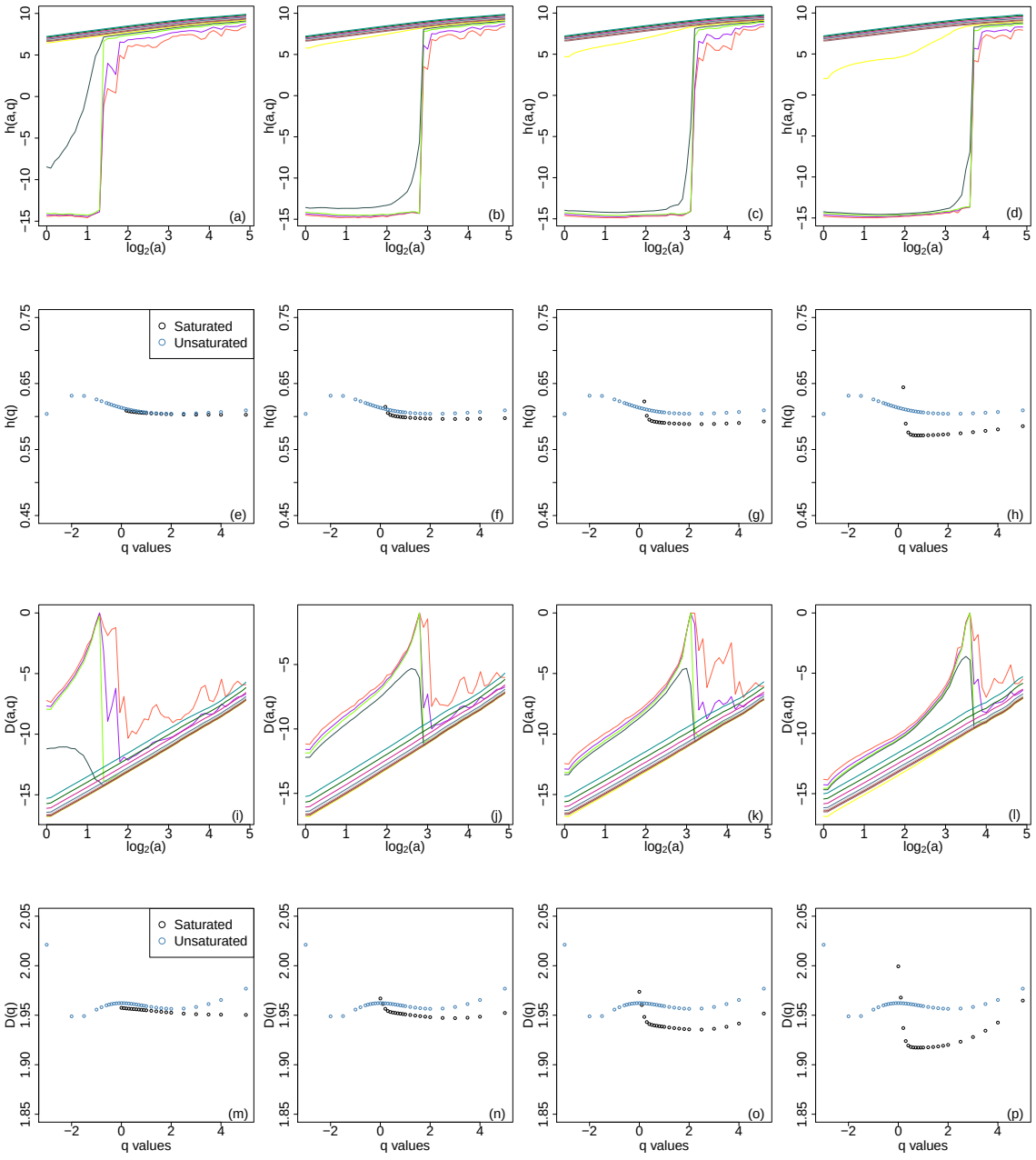

Figure 3.3: Each column has the same structure, the first row is the $h(a,q)$ plot followed by $h(q)$, $D(a,q)$ and $D(q)$. The first column is for saturation at the 1% level followed by 5%,10% and 20% levels. The colors corresponds to the different q values as described in the legend in Figure 3.1d. Image saturation reduces the range of statistical order moments because of the lack of a good power law fit in the $h(a,q)$ and $D(a,q)$ plots. Thus in the corresponding $h(q)$ and $D(q)$ plots there are less statistics for saturated images (black dots).

The last two rows of Figure 3.3 ($D(a,q)$ and $D(q)$ plots) followed a similar procedure as the $h(a,q)$ and $h(q)$ plots. It is clear that image saturation affects the output statistics of the 2D WTMM method. In the next section, we explain the rescue method and its ability to recapture lost statistical order moments.

3.3 The Rescue Method

As mentioned in the Introduction, the rescue method is a novel technique that was developed by exploring the effects of saturation; it did not exist in the previous literature. Specifically we constructed a filtering approach of the sheaves that reduces the impact of image saturation, and recaptures lost q values. In similar style, we will only discuss the long-range correlated ($H = 0.7$) fBm surfaces, without loss of generality. The rescue method's filtering approach is similar for all fBm surfaces, only the parameter coefficients change.

We noticed the impact, as mentioned before, early on in the sheaves of saturated images displayed in Figure 3.2, these corrupted sheafs would affect the $h(a,q)$ and $D(a,q)$ plots. We developed a filter approach based upon the modulus value and "adjusted" slope of the maxima line where MF corresponds to the modulus filter while SF corresponds to the slope filter.

Definition 3.3.1. Let $l \in \mathcal{L}(a)$ be a maxima line ending at scale a_{max}, where $\mathcal{M}_{l(a=a')}$ is the value of the modulus for maxima line l at scale a', we define the adjusted slope as:

$$m_{adj} = \frac{\mathcal{M}_{l(a=0)} - \mathcal{M}_{l(a=a_{max})}}{\mathcal{M}_{l(a=a_{max})}}.$$

zo To calculate m_{adj} one takes the starting modulus value of a maxima line (scale 0) and subtracts the ending modulus value all divided by the ending modulus value. When working with SF, all maxima lines that satisfied $m_{adj} \leq SF$ were kept.

In this section, any red coloring corresponds to maxima that were removed from thresholding on the modulus, while green corresponds to maxima removed from the slope filtering. Setting the modulus threshold was straight forward however the adjusted slope threshold required more simulations. From comparing saturated sheaves with normal sheaves we determined that any maxima lines with a value of 16 (2^4) or less should be removed. Figure 3.4 illustrates the data mining approach that we took to determine the optimal filtering coefficients. For all three columns in Figure 3.4 $MF = 16$, with $SF = 0.2, 0.5, 0.8$ in order to show how the sloping parameter functioned; the goal was to remove the maxima lines that caused the saturated sheaf to look different from an unsaturated sheaf. For instance in Figure 3.4g the resulting filtered saturated sheaf has maxima lines that are truncated while Figure 3.4i has many negative sloping, low valued maxima lines compared to the unsaturated case. Figure 3.4h displays what was determined to be the optimal filtering coefficients. Figure 3.4j is a sheaf on an unsaturated fBm surface with $H = 0.7$ and was the benchmark.

The filtering parameters selected were $MF = 16$ and $SF = 0.5$ which are displayed in Figure 3.4. Figure 3.6 shows the effect of the rescue method on the WT skeleton. These pruned sheaves were then passed to the partition functions to make the $h(a, q)$ and $D(a, q)$ plots. Figure 3.5 shows this for $H = 0.7$ and $S = 0.20$, we can see the lack of stair step behavior in the Figures 3.5a and 3.5b compared to their saturated counterparts in Figure 3.3l and 3.3d. With more curves providing a good power law fit we are able to expand the range of statistical order moments displayed in Figure 3.5. For reference, the saturated images had a q range of $0.1 < q \leq 5$ with the rescue method the range was expanded to $-2 \leq q < 5$.

3.4 Final Remarks

The rescue method, with a slight adjustment in values, works for the other fractional Brownian surfaces for all the saturation levels. We also tested the rescue method on

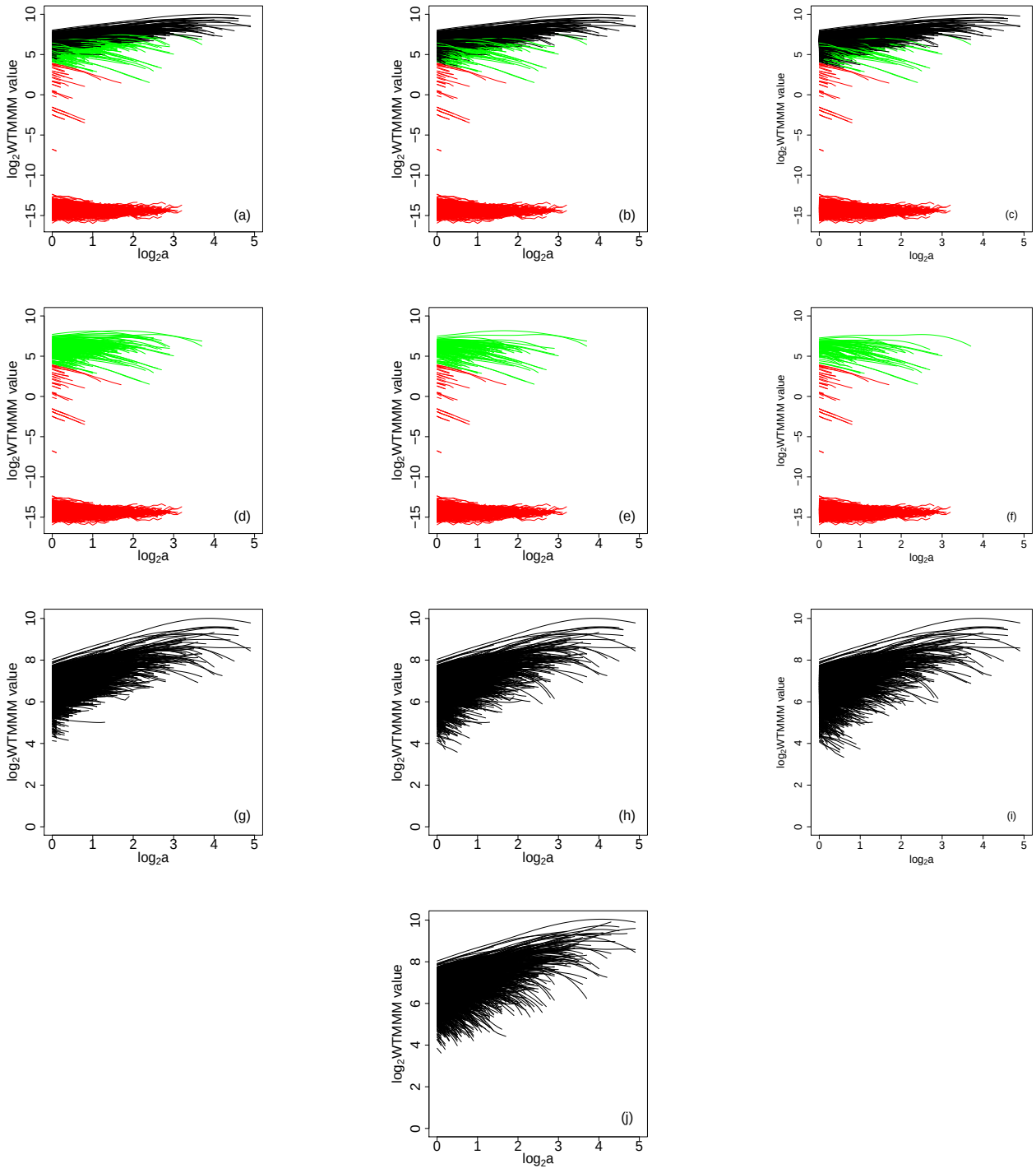

Figure 3.4: This is an example of the data mining approach to isolate the optimal values for MF and SF. All three columns have $MF = 16$ while the left most has $SF = 0.2$ and the right most $SF = 0.8$. (j) is unsaturated sheaf.

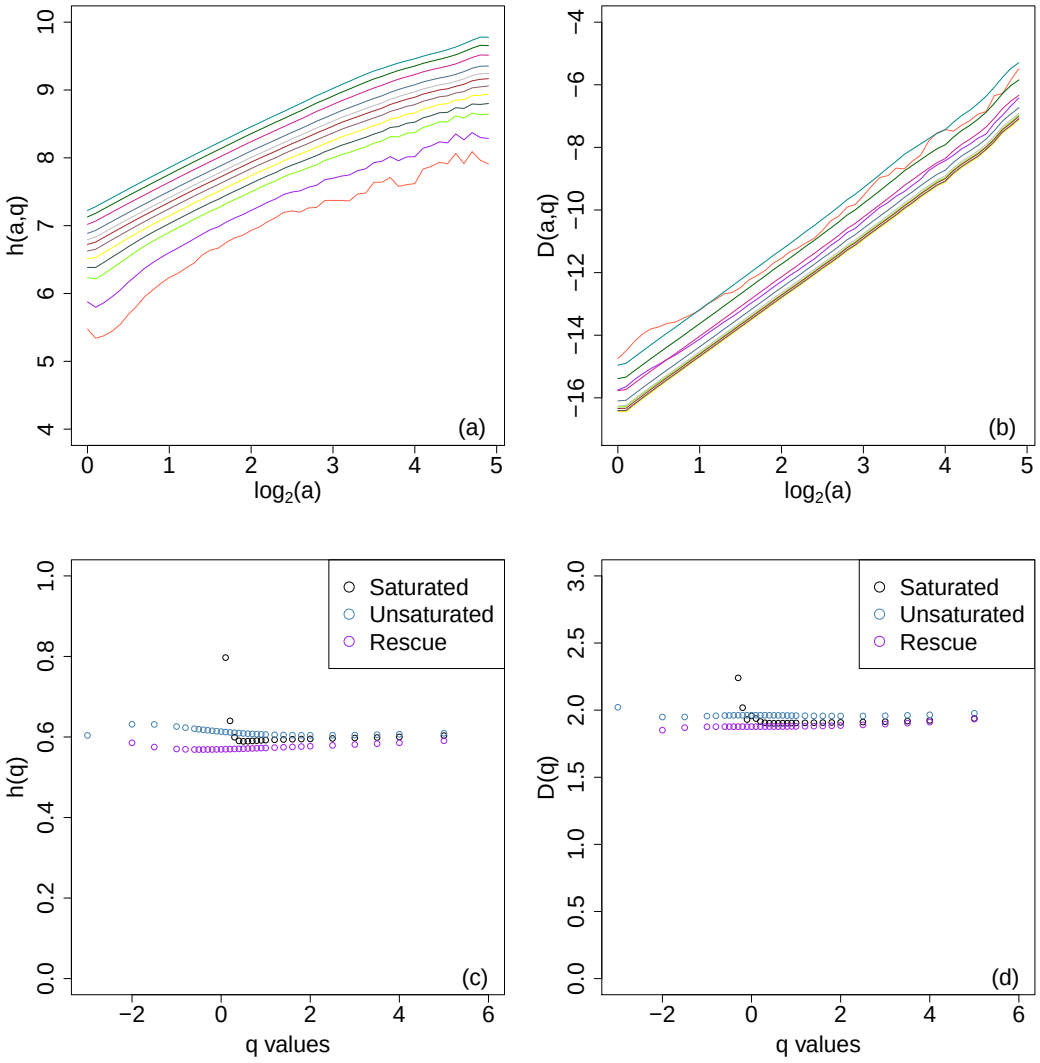

Figure 3.5: These graphs show the efficacy of the rescue method. The $h(a,q)$ and $D(a,q)$ plots have better power law fits for a wider range of statistical order moments relative to their saturated counterparts. This expanded range of q values is reflected in the $h(q)$ and $D(q)$ plots. The saturated images had a q range $0.1 < q < 5$ while the rescue method had $-2 \leq q \leq 5$.

unsaturated fractional Brownian motion surfaces, and saw minimal impact on the statistics displayed in Figure 3.7. This shows that the method does not have unintended effects on normal fBm surfaces. The black dots are normal fBms while the blue dots are the same set of normal images but with the rescue method applied. Lastly Figure 3.8 shows the difference in the statistical order moment range in saturated and rescued images. The figure shows the efficacy of the rescue method and we will be able to recover some of the

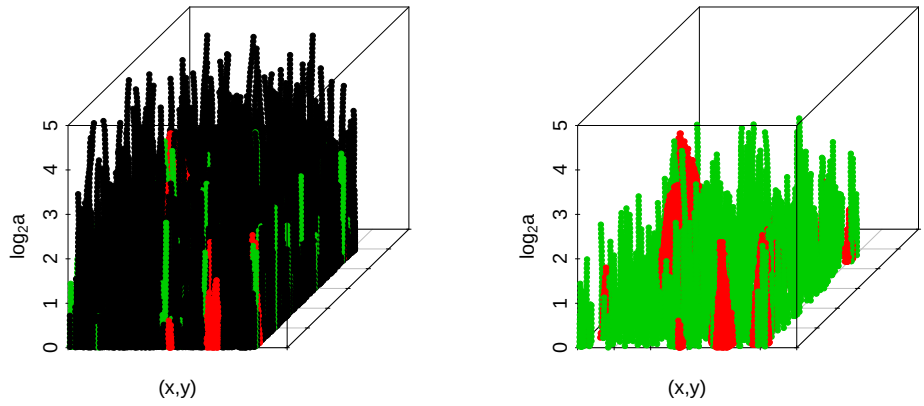

Figure 3.6: The red dots correspond to maxima lines that were removed from $MF = 16$ and the green dots are the maxima lines that were removed from $SF = 0.5$.

gray image subregions in Figure 1.1, thus reducing the impact of image saturation. Moreover, nearly the entire range of q values is recaptured which gives more statistics to describe the underlying image. Future work includes developing techniques for other image artifacts that impact the analysis.

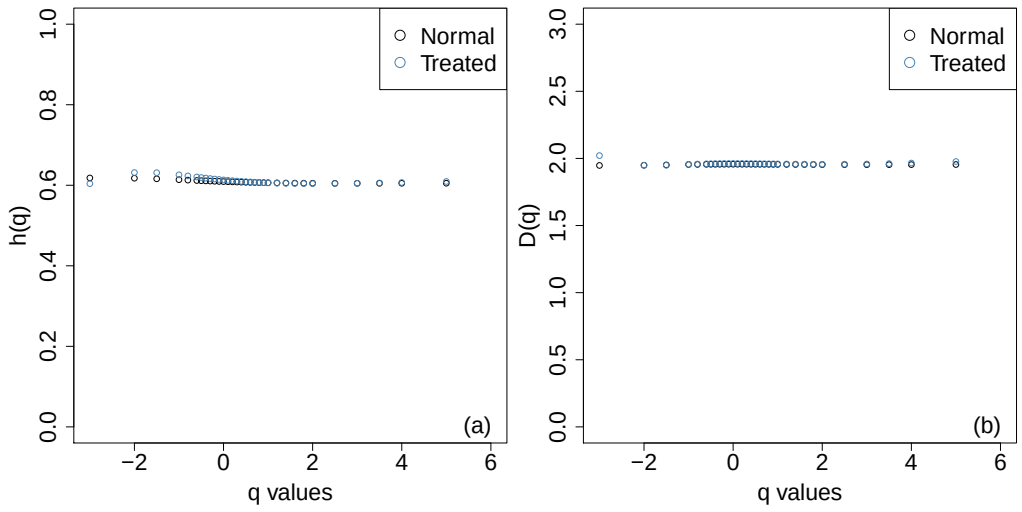

Figure 3.7: These graphs show the lack of effect of the rescue method on normal unsaturated fractional Brownian surfaces. The statistics remain about the same.

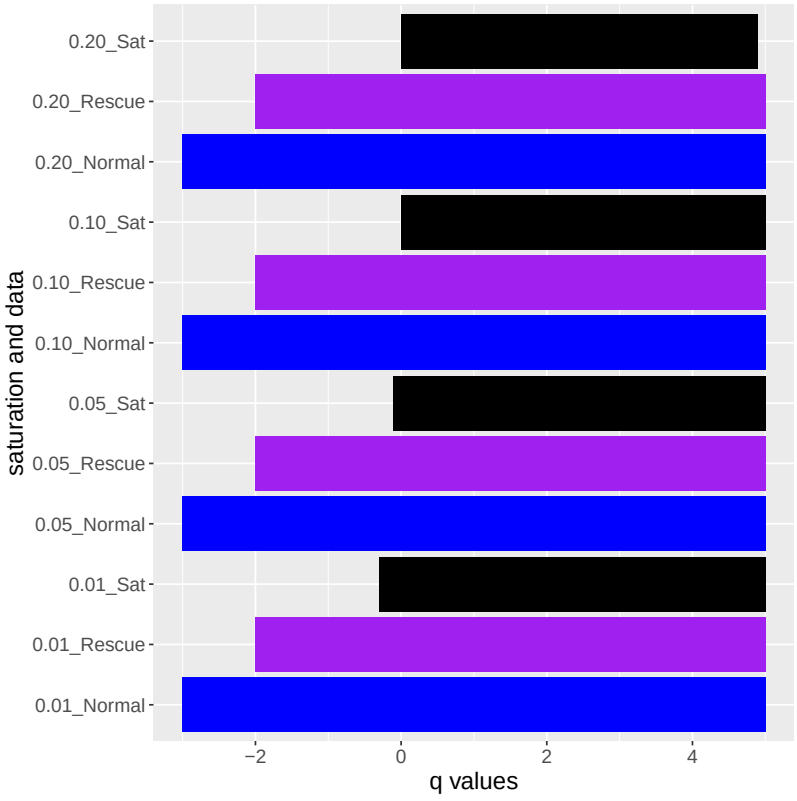

Figure 3.8: The larger the bar, the wider the range of statistical order moments for fBm surfaces with $H = 0.7$. The rescued method consistently provided a wider range of q values compared to the saturated images.

REFERENCES

[1] A Arneodo, B Audit, N Decoster, J Muzy, and C Vaillant. Wavelet based multifractal formalism: applications to dna sequences, satellite images of the cloud structure, and stock market data. In *The science of Disasters*, pages 26–102. Springer, 2002.

[2] A Arneodo, N Decoster, and S Roux. A wavelet-based method for multifractal image analysis. I. methodology and test applications on isotropic and anisotropic random rough surfaces. *The European Physical Journal B-Condensed Matter and Complex Systems*, 15(3):567–600, 2000.

[3] M Barnsley. *Fractals everywhere*. Academic Press Professional, Boston, MA, second edition, 1993.

[4] K Batchelder, A Tanenbaum, S Albert, L Guimond, P Kestener, A Arneodo, and A Khalil. Wavelet-based 3d reconstruction of microcalcification clusters from two mammographic views: new evidence that fractal tumors are malignant and euclidean tumors are benign. *PloS one*, 9(9), 2014.

[5] M Bissell and W Hines. Why don't we get more cancer? a proposed role of the microenvironment in restraining cancer progression. *Nature medicine*, 17(3):320, 2011.

[6] G Casella and R Berger. *Statistical inference*. The Wadsworth & Brooks/Cole Statistics/Probability Series. Wadsworth & Brooks/Cole Advanced Books & Software, Pacific Grove, CA, 1990.

[7] N Decoster, S Roux, and A Arneodo. A wavelet-based method for multifractal image analysis. II. applications to synthetic multifractal rough surfaces. *The European Physical Journal B-Condensed Matter and Complex Systems*, 15(4):739–764, 2000.

[8] L Eadie, P Taylor, and A Gibson. A systematic review of computer-assisted diagnosis in diagnostic cancer imaging. *European journal of radiology*, 81(1):e70–e76, 2012.

[9] K Falconer. *Fractal geometry*. John Wiley & Sons, Ltd., Chichester, third edition, 2014. Mathematical foundations and applications.

[10] J Fenton, L Abraham, S Taplin, B Geller, P Carney, C D'Orsi, J Elmore, W Barlow, and Breast Cancer Surveillance Consortium. Effectiveness of computer-aided detection in community mammography practice. *Journal of the National Cancer institute*, 103(15):1152–1161, 2011.

[11] J Fenton, S Taplin, P Carney, L Abraham, E Sickles, C D'Orsi, E Berns, G Cutter, E Hendrick, W Barlow, et al. Influence of computer-aided detection on performance of screening mammography. *New England Journal of Medicine*, 356(14):1399–1409, 2007.

[12] J Fenton, G Xing, J Elmore, H Bang, S Chen, K Lindfors, and L Baldwin. Short-term outcomes of screening mammography using computer-aided detection: a population-based study of medicare enrollees. *Annals of internal medicine*, 158(8):580–587, 2013.

[13] Thomas C. Halsey, Mogens H. Jensen, Leo P. Kadanoff, Itamar Procaccia, and Boris I. Shraiman. Fractal measures and their singularities: the characterization of strange sets. *Phys. Rev. A (3)*, 33(2):1141–1151, 1986.

[14] A Khalil. Biomedical image analysis. University Lecture Slides, 2019.

[15] A Khalil, C Aponte, R Zhang, T Davisson, I Dickey, D Engelman, M Hawkins, and M Mason. Image analysis of soft-tissue in-growth and attachment into highly porous alumina ceramic foam metals. *Medical engineering & physics*, 31(7):775–783, 2009.

[16] A Khalil and K Batchelder. Improved methods of cancer detection, U.S. Patent 10 467 755B2, 2019.

[17] A Khalil, G Joncas, F Nekka, P Kestener, and A Arnéodo. Morphological analysis of hi features. II. wavelet-based multifractal formalism. *The Astrophysical Journal Supplement Series*, 165(2):512, 2006.

[18] S Kim, W Moon, M Seong, N Cho, and J Chang. Computer-aided detection in digital mammography: false-positive marks and their reproducibility in negative mammograms. *Acta Radiologica*, 50(9):999–1004, 2009.

[19] C Lehman, R Wellman, D Buist, K Kerlikowske, A Tosteson, and D Miglioretti. Diagnostic accuracy of digital screening mammography with and without computer-aided detection. *JAMA internal medicine*, 175(11):1828–1837, 2015.

[20] J Louro, M Posso, M Boon, M Román, L Domingo, X Castells, and M Sala. A systematic review and quality assessment of individualised breast cancer risk prediction models. *British journal of cancer*, 121(1):76–85, 2019.

[21] S Mallat. *A wavelet tour of signal processing*. Academic Press, Inc., San Diego, CA, 1998.

[22] B Mandelbrot. *The fractal geometry of nature*, volume 173. WH freeman New York, 1983.

[23] B Mandelbrot and J Van Ness. Fractional Brownian motions, fractional noises and applications. *SIAM review*, 10(4):422–437, 1968.

[24] Z Marin, K Batchelder, B Toner, L Guimond, E Gerasimova-Chechkina, A Harrow, A Arneodo, and A Khalil. Mammographic evidence of microenvironment changes in tumorous breasts. *Medical physics*, 44(4):1324–1336, 2017.

[25] M Noble, W Bruening, S Uhl, and K Schoelles. Computer-aided detection mammography for breast cancer screening: systematic review and meta-analysis. *Archives of gynecology and obstetrics*, 279(6):881–890, 2009.

[26] R Pool. Artificial intelligence: Best for breast, 2018.

[27] S Roux, A Arneodo, and N Decoster. A wavelet-based method for multifractal image analysis. III. applications to high-resolution satellite images of cloud structure. *The European Physical Journal B-Condensed Matter and Complex Systems*, 15(4):765–786, 2000.

[28] M Sak, P Littrup, N Duric, M Mullooly, M Sherman, and G Gierach. Current and future methods for measuring breast density: a brief comparative review. *Breast cancer management*, 4(4):209–221, 2015.

[29] G Shevchenko. Fractional Brownian motion in a nutshell. In *Analysis of fractional stochastic processes*, volume 36 of *Int. J. Modern Phys. Conf. Ser.*, pages 1560002, 16. World Sci. Publ., Hackensack, NJ, 2015.

[30] J Stewart. Multivariable calculus early transcendental, 2003.

[31] K Tanner, H Mori, R Mroue, A Bruni-Cardoso, and M Bissell. Coherent angular motion in the establishment of multicellular architecture of glandular tissues. *Proceedings of the National Academy of Sciences*, 109(6):1973–1978, 2012.

BIOGRAPHY OF THE AUTHOR

An intrigue of wavelets and fractals brought him to the University of Maine so he could work with Dr. Andre Khalil whose specialty is such. He also works with the CompuMAINE lab in developing metrics for image colocalization that offer different insights than the standard, off-the-shelf algorithms. Jeremy enjoys the programming and interdisciplinary nature of the research. He is also the founder of the machine learning subgroup within CompuMAINE. He will begin a PhD program in Electrical and Computer Engineering at the University of Maine in Fall 2020.

LinkedIn Profile: `https://www.linkedin.com/in/jeremyjuybari`

Personal website: `https://jjuybari.com/`

Jeremy Bijan Juybari is a candidate for the Master of Arts degree in Mathematics from the University of Maine in May 2020.